Time-of-flight PET time calibration using data consistency.

Michel Defrise[1], **Ahmadreza Rezaei**[2], **Johan Nuyts**[3]

Abstract

This paper presents new data driven methods for the time of flight (TOF) calibration of positron emission tomography (PET) scanners. These methods are derived from the consistency condition for TOF PET, they can be applied to data measured with an arbitrary tracer distribution and are numerically efficient because they do not require a preliminary image reconstruction from the non-TOF data. Two-dimensional simulations are presented for one of the methods, which only involves the two first moments of the data with respect to the TOF variable. The numerical results show that this method estimates the detector timing offsets with errors that are larger than those obtained via an initial non-TOF reconstruction, but remain smaller than 10% of the TOF resolution and thereby have a limited impact on the quantitative accuracy of the activity image estimated with standard maximum likelihood reconstruction algorithms.

[1]Dept. of Nuclear Medicine, Vrije Universiteit Brussel, B-1090, Brussels, Belgium,
mail: mdefrise@vub.ac.be,
[2]Dept. of Nuclear Medicine, KU Leuven, B-3000, Leuven, Belgium,
mail: ahmadreza.rezaei@uzleuven.be,
[3]Dept. of Nuclear Medicine, KU Leuven, B-3000, Leuven, Belgium,
mail: johan.nuyts@uzleuven.be.

1. Introduction

Image reconstruction from time-of-flight PET data requires an accurate calibration of the time-of-flight measurements. This calibration is usually done by measuring a known activity distribution such as a rotating rod source, a point source, or a shell [1, 2, 3, 4]. Alternative, data driven methods are useful when the precise geometry or positioning of the calibration source is not known, or when one wishes to monitor possible drifts of the TOF offsets directly from clinical data. A simple and efficient data driven method [5] is the *indirect method*: it exploits the fact that the non-TOF data obtained by summing the measured data over all time bins are not affected by possible timing errors. Reconstructing and then forward projecting the non-TOF data yields for each line of response (LOR) a synthetic TOF profile which can be aligned with the measured one. A similar data driven method jointly estimates the activity distribution and the time alignement using alternate likelihood optimization [6].

This work explores *direct* data driven methods for TOF calibration, which do not require a preliminary non-TOF reconstruction, are faster, and could in some cases be applied to incomplete data. The approach is motivated by the observation that the difference between the TOF profiles measured for two neighboring LORs is caused both by a possible time misalignment and by the local variation of the object. A time misalignment results in a global shift of the TOF profile, which can be disentangled from the more structured differences due to the object. This paper translates this intuition into mathematically rigorous relations. Note that simpler data driven methods can be used if additional information is available. For instance, the position and orientation of a calibration source with known shape, such as a flood source, can be estimated directly from the data, enabling next a straightforward estimation of the TOF offset of each LOR [7].

We consider a continuous 2D model of the problem, assuming as in [1, 2, 3, 4, 5] that the TOF misalignment of each LOR is equal to the difference between the timing offsets of the two detectors in coincidence. The consistency equations for TOF PET are used in section 3 to derive a quadratic differential equation linking the PET data to the detector offsets. Rather than directly solving this equation, we integrate it first over to the TOF variable (section 4) and then over the fan angle (section 5). This leads to a simple relation between the data and the detector offsets, which is linear, only involves the two first moments of the TOF data, and is independent of the TOF resolution.

The proposed method is based on a continuous analytic model and therefore is only applicable provided the data sampling is sufficiently fine. When this condition holds, the discrete implementation is straightforward as described in section 6. Numerical results with simulated 2D data in section 7 show that this consistency based TOF calibration method does not match the accuracy of the indirect method, but nevertheless recovers the detector timing offsets with errors that are small compared to the TOF resolution. This lower accuracy has a limited impact on the activity image estimated with standard maximum likelihood reconstruction algorithms. As shown in [6] however, a higher accuracy is needed for other problems such as the joint estimation of activity and attenuation.

2. The consistency condition for fan-beam TOF PET data

The native parameterization for PET data in a single ring scanner uses the angular coordinates α, β of the two detectors in coincidence. This section defines notations and introduces the consistency conditions for this fan-beam parametrization.

Consider a circular detector ring of radius R and the LOR connecting two detectors located at $\vec{a} = (R\cos\alpha, R\sin\alpha)$ and $\vec{b} = (R\cos\beta, R\sin\beta)$. The LOR length is denoted

$$L = \|\vec{a} - \vec{b}\| = 2R\,|\sin(\frac{\beta - \alpha}{2})|, \tag{1}$$

omitting the dependence on α, β to simplify notations. The ideal TOF data, normalized for detector efficiency and corrected for attenuation and background, are

$$q(\alpha, \beta, t) = \int dl\, w(t - l)\, f\Big(\frac{\vec{a} + \vec{b}}{2} - l\frac{\vec{a} - \vec{b}}{L}\Big), \quad (\alpha, \beta, t) \in \mathcal{D} \tag{2}$$

where the activity distribution f is assumed to be continuously differentiable and $w(t)$ is a gaussian TOF profile with known standard deviation $\sigma < \infty$,

$$w(t) = e^{-t^2/2\sigma^2}/\sqrt{2\pi}\sigma. \tag{3}$$

The TOF variables in this paper are all converted to lengths (in mm). The argument of f in (2) is $\vec{a}$ when $l = -L/2$, therefore the first argument of q, α, will always correspond to the detector at $t < 0$. This detector is in coincidence with a fan of detectors $\alpha + \pi - \Phi \leq \beta \leq \alpha + \pi + \Phi$, where the fan aperture $\Phi < \pi$ defines the field-of-view radius $R_{FOV} = R\sin(\Phi/2)$. We consider to simplify notations a redundant sampling domain

$$\mathcal{D} = [0, 2\pi) \times (\alpha + \pi - \Phi, \alpha + \pi + \Phi) \times (t_{min}, t_{max}) \tag{4}$$

with the identification $q(\alpha, \beta, t) = q(\beta, \alpha, -t)$. Note that $\sin((\beta - \alpha)/2) > 0$ for $(\alpha, \beta, t) \in \mathcal{D}$.

Equation (2) admits a solution f only if the data satisfy the following consistency condition

$$\begin{aligned} 0 = t\left(\frac{\partial q}{\partial \alpha} - \frac{\partial q}{\partial \beta}\right)\frac{1}{\sin((\beta - \alpha)/2)} + \zeta(\alpha, \beta)R\left(\frac{\partial q}{\partial \alpha} + \frac{\partial q}{\partial \beta}\right) \\ - R^2\cos((\beta - \alpha)/2)\frac{\partial q}{\partial t} + \sigma^2\left(\frac{\partial^2 q}{\partial \alpha \partial t} - \frac{\partial^2 q}{\partial \beta \partial t}\right)\frac{1}{\sin((\beta - \alpha)/2)} \end{aligned} \tag{5}$$

with $\zeta(\alpha, \beta) = sign(\sin((\beta - \alpha)/2))$. We denote below the RHS of (5) as $\mathcal{E}q$. Equation (5) is equivalent to the consistency condition for PET data parametrized using sinogram coordinates, and can be derived from the latter by applying a change of coordinate

$(s,\phi) \to (\alpha,\beta)$ to equation (2) in [8] or equation (8) in [9]. A direct proof is given for completeness in Appendix 1.

3. A differential equation for the detector offsets

Suppose that the detector at angular position α has a TOF offset $\eta(\alpha) \in C^1(0,2\pi)$. We assume with Werner and Karp [5] that the TOF offset for each LOR is the difference between the TOF offsets of the two detectors in coincidence. The measured data (normalized and corrected for attenuation and background) are then related to the ideal data by $m(\alpha,\beta,t) = q(\alpha,\beta,t-\eta(\alpha)+\eta(\beta))$. Applying to m the operator $\mathcal{E}$ defined by (5), and using the fact that $\mathcal{E}q = 0$, we obtain (proof in Appendix 2):

$$\begin{aligned} \sin((\beta-\alpha)/2)\,\mathcal{E}m &= (\eta(\alpha)-\eta(\beta))\left(\frac{\partial m}{\partial\alpha}-\frac{\partial m}{\partial\beta}\right) \\ &+ (\eta(\alpha)-\eta(\beta)-t)(\eta'(\alpha)+\eta'(\beta))\frac{\partial m}{\partial t} - \sigma^2(\eta'(\alpha)+\eta'(\beta))\frac{\partial^2 m}{\partial t^2} \\ &- R\,|\sin((\beta-\alpha)/2)|\,(\eta'(\alpha)-\eta'(\beta))\frac{\partial m}{\partial t} \end{aligned} \tag{6}$$

where $\eta'(\alpha) = d\eta(\alpha)/d\alpha$ and the argument of m and its derivatives is (α,β,t). Note that this equation is non-linear due to the product $(\eta(\alpha)-\eta(\beta)-t)(\eta'(\alpha)+\eta'(\beta))$.

Grouping equation (6) for all data bins $(\alpha,\beta,t) \in \mathcal{D}$ yields a large system of equations, which could in principle be solved jointly for all detector offsets $\eta(\alpha), 0 \leq \alpha < 2\pi$. Two more practical approaches are derived in the following sections.

4. A TOF-summed consistency equation for the detector offsets

We assume from now on that the sampled TOF interval t_{min}, t_{max} covers the (essential) support of the function m, i.e. we assume that $m(\alpha,\beta,t)$ and all its derivatives are zero at $t = t_{max}$ and $t = t_{min}$. Integrating (6) over t and using partial integration removes the terms with second derivatives and the non-linear term, and results in a simple relation linking the measured data to the detector offsets η (proof in Appendix 3):

$$\begin{aligned} &\left(\frac{\partial M_1}{\partial\alpha}-\frac{\partial M_1}{\partial\beta}\right) + R\,|\sin((\beta-\alpha)/2)|\left(\frac{\partial M_0}{\partial\alpha}+\frac{\partial M_0}{\partial\beta}\right) \\ &= (\eta(\alpha)-\eta(\beta))\left(\frac{\partial M_0}{\partial\alpha}-\frac{\partial M_0}{\partial\beta}\right) + (\eta'(\alpha)+\eta'(\beta))M_0 \\ &= \left(\frac{\partial}{\partial\alpha}-\frac{\partial}{\partial\beta}\right)\{(\eta(\alpha)-\eta(\beta))M_0(\alpha,\beta)\} \end{aligned} \tag{7}$$

where we defined the first two moments of the data with respect to the TOF variable,

$$M_i(\alpha,\beta) = \int_{t_{min}}^{t_{max}} dt\, t^i\, m(\alpha,\beta,t) \quad i = 0,1. \tag{8}$$

Define the set of sampled LORs with measured activity exceeding some threshold ϵ:

$$\mathcal{L}_\epsilon = \{(\alpha,\beta) \,|\, M_0(\alpha,\beta) \geq \epsilon\}\,. \tag{9}$$

Grouping equation (7) for all LORs $(\alpha,\beta) \in \mathcal{L}_\epsilon$ yields a system of equations for the detector offsets. This system of equations is linear in η -therefore easy to solve- but the calibration problem remains intrinsically non-linear because both the LHS and the coefficients of η and η' in the RHS depend on the data.

We observed with a preliminary implementation on simulated data that the solution of (7) tends to be biased in presence of noise, and we tentatively attribute this bias to the non-linearity of the problem. As shown in the following section, a second integration of the consistency equation with respect to the fan-angle eliminates the terms involving derivatives of the data and strongly reduces the bias.

Remark 1. Equation (7) only involves the first two moments M_0 and M_1 of the data and the simplification compared to the full non-linear relation (6) potentially entails a loss of information. However higher moments (i.e. M_l with $l > 1$) are expected to be increasingly sensitive to noise, and we conjecture that the loss of information is limited.

5. A fan-summed consistency equation for the detector offsets

We assume as in section 4 that the sampled TOF interval t_{min}, t_{max} covers the (essential) support of the function m. We make the additional assumption that the fan covers the object, hence $M_l(\alpha,\beta)$ and all its derivatives are zero at $\beta = \alpha + \pi \pm \Phi$. This new assumption prevents direct application if the detector ring has gaps or if the object is larger than the FOV. Application in presence of gaps will be discussed in section 6.1.

Fixing α and integrating the TOF-summed equation (7) over β leads to the following invariance property (proof in Appendix 4):

$$\int_{\alpha+\pi-\Phi}^{\alpha+\pi+\Phi} d\beta \,\{M_1 - (\eta(\alpha) - \eta(\beta))M_0 + R\,|\sin((\beta-\alpha)/2)|M_0\} = C \tag{10}$$

where C is a constant independent of α, which can be determined by integrating (10) over $0 \leq \alpha < 2\pi$, and by noting that

$$\begin{aligned}&\int_0^{2\pi} d\alpha \int_{\alpha+\pi-\Phi}^{\alpha+\pi+\Phi} d\beta \,\{M_1(\alpha,\beta) - (\eta(\alpha) - \eta(\beta))M_0(\alpha,\beta)\}\\ &= \int_0^{2\pi} d\alpha \int_0^{2\pi} d\beta \,\{M_1(\alpha,\beta) - (\eta(\alpha) - \eta(\beta))M_0(\alpha,\beta)\} = 0.\end{aligned} \tag{11}$$

The first equality in equation (11) is obtained by extending the data to $[0,2\pi) \times [0,2\pi)$ by setting $M_0(\alpha,\beta) = M_1(\alpha,\beta) = 0$ for LORs outside the field-of-view and the second equality follows from the symmetries $M_0(\alpha,\beta) = M_0(\beta,\alpha)$ and $M_1(\alpha,\beta) = -M_1(\beta,\alpha)$. Therefore,

$$2\pi C = \int_0^{2\pi} d\alpha \int_{\alpha+\pi-\Phi}^{\alpha+\pi+\Phi} d\beta \, R\,|\sin((\beta-\alpha)/2)|M_0(\alpha,\beta). \tag{12}$$

The detector offsets are therefore solution of a linear integral equation of the second type [17, 18]:

$$T(\alpha)\,\eta(\alpha) = F(\alpha) + \int_0^{2\pi} d\beta\, K(\alpha,\beta)\eta(\beta) \quad 0 \le \alpha < 2\pi \tag{13}$$

with the fan- and TOF-summed data

$$T(\alpha) = \int_0^{2\pi} d\beta\, M_0(\alpha,\beta), \tag{14}$$

the function

$$F(\alpha) = -C + \int_0^{2\pi} d\beta\ \{M_1(\alpha,\beta) + R\,|\sin((\beta-\alpha)/2)| M_0(\alpha,\beta)\}\,, \tag{15}$$

with C given by (12), and the integral kernel

$$K(\alpha,\beta) = \begin{cases} M_0(\alpha,\beta) & |\beta-\alpha-\pi| < \Phi \\ 0 & |\beta-\alpha-\pi| \ge \Phi. \end{cases} \tag{16}$$

Under general assumptions, we prove in Appendix 5 that equation (13) has a unique solution $\eta(\alpha), 0 \le \alpha < 2\pi$ up to an additive constant, which does not affect the LOR offsets $\eta(\alpha) - \eta(\beta)$ required for image reconstruction.

Remark 2. Suppose estimates $\hat{\chi}(\alpha,\beta)$ of the LOR offsets are obtained from a standard calibration method with a known source, or using the indirect method. The detector offsets can then be calculated by solving $\hat{\chi}(\alpha,\beta) = \eta(\alpha) - \eta(\beta)$ for η. One easily verifies that solving this equation by weighted least-squares estimation with weights equal to the LOR activity M_0 leads to the same equation as (13), with $T(\alpha)$ also given by (14), and with

$$F(\alpha) = \int d\beta\, M_0(\alpha,\beta)\hat{\chi}(\alpha,\beta). \tag{17}$$

The consistency condition can therefore be seen as a method to calculate the integral (17) directly from the pre-corrected TOF data of an arbitrary source of activity.

6. Discretization

We consider a circular ring scanner of radius R with $2N$ equally spaced detectors, and sample the measured data as m_{j,k,i_t} with TOF sampling Δ_t:

$$\begin{aligned} \alpha_j &= j\pi/N \quad j = 0,\ldots,2N-1 \\ \beta_{j,k} &= \alpha_j + \pi + k\pi/N \quad -k_{max} \le k \le k_{max} \\ t &= i_t\,\Delta_t \quad i_t = -i_m,\ldots,i_m \end{aligned} \tag{18}$$

so that $\{\beta_{j,k}, |k| \le k_{max}\}$ is the fan of detectors in coincidence with detector α_j. The fan aperture is chosen as

$$N > k_{max} \ge \frac{2N}{\pi} \arcsin(R_{FOV}/R). \tag{19}$$

Note that

$$\frac{\beta_{j,k} - \alpha_j}{2} = \frac{\pi}{2N}(N+k) \in [0,\pi). \tag{20}$$

For easier implementation, we store the data according to (18). As noted in section 2 this sampling is redundant because each LOR is stored twice with $m_{j,k,i_t} = m_{j',-k,-i_t}$ with $j' = (j + N + k)\%2N$. This redundance has no impact on the numerical results. The data moments are calculated as $M_{0,j,k} = \sum_{i_t} m_{j,k,i_t}$ and $M_{1,j,k} = \Delta_t \sum_{i_t} i_t \, m_{j,k,i_t}$.

6.1. Implementation of equation (13)

We discretize the integrals over α using the trapezoidal method,

$$\int d\alpha \simeq \sum_j \Delta_j$$

where Δ_j is the weight of detector j at α_j. The weights are constant in the absence of gaps, $\Delta_j = \pi/N$. In the presence of gaps the weights of the two detectors surrounding each gap are modified as follows. If the detectors j_a and $j_b = j_a + w + 1$, are separated by a gap of w missing detectors, their weights are set to $\Delta_{j_a} = \Delta_{j_b} = (1 + w/2)\pi/N$ and the weights in the gap are set to zero: $\Delta_j = 0, j = j_a + 1, \ldots, j_b - 1$.

Sampling the fan- and TOF-summed equation (13) at α_j with this trapezoidal integration leads to a system of linear equations $U \cdot \eta = Y$, with the $2N \times 2N$ matrix U with elements

$$U_{j_1,j_2} = T_{j_1} \delta_{j_1,j_2} - \Delta_{j_2} \, M_{0,j_1,k} \quad j_1, j_2 = 0, \cdots, 2N - 1 \tag{21}$$

where δ is the Kronecker delta, $k = -N + (j_2 - j_1)\%(2N)$ is the fan index of the LOR (j_1, j_2), and we extend the data by $M_{0,j_1,k} = 0$ if $|k| > k_{max}$ or if the LOR (j_1, k) is in a gap. The diagonal term is $T_{j_1} = \sum_k \Delta_{j_2} \, M_{0,j_1,k}$.

The right hand side vector is

$$Y_{j_1} = -C + \sum_{k=-k_{max}}^{k_{max}} \Delta_{j_2} \left(M_{1,j_1,k} + R \left| \sin\left(\frac{\pi(N+k)}{2N}\right) \right| M_{0,j_1,k} \right) \quad j_1 = 0, \cdots, 2N-1 \tag{22}$$

with $j_2 = (j_1 + N + k)\%(2N)$ and C such that $\sum_{j_1} \Delta_{j_1} Y_{j_1} = 0$.

The matrix U is singular because the offsets η are determined only up to a constant and also (with gaps) because all entries corresponding to missing detectors are zero. To avoid indeterminacy we add a diagonal matrix $\mu \, \lambda_{max} \, Id$ to U, with Id the identity matrix, $\mu = 10^{-5}$ and λ_{max} the largest eigenvalue of U. The system $(U + \mu \, \lambda_{max} \, Id) \cdot \eta = Y$ is then solved for η by gaussian elimination (*gaussj* from [19]). Offsets estimated for missing detectors are of course discarded.

6.2. Smoothing M_0

For noisy data, the TOF summed data M_0 are smoothed before applying equation (13). We apply a three point smoothing kernel $(0.3, 0.4, 0.3)$ at fixed fan angle k so as to minimize the distance between the three averaged LORs at the center of the FOV. A two point kernel is used for detectors at the edge of a gap. Note that the first moment M_1 is affected by the timing misalignement and must not be smoothed.

6.3. Implementation of the indirect method [5]

The non-TOF reconstruction is obtained using OSEM with a Joseph projector [10] and matched backprojector, with an image pixel size approximately equal to the ray spacing at the center of the field-of-view (this choice minimizes artefacts caused by the use of a line integral projector and matched backprojector). For numerical consistency the non-TOF reconstruction is here implemented as a TOF reconstruction with a FWHM set at 5250 mm (but a true non-TOF reconstruction was used to estimate the computation time in section 7.4). The TOF projections of the non-TOF image are calculated using the same projector, to yield for each LOR a discrete TOF profile $q_{j,k,i_t}, i_t = -i_m, \ldots, i_m$. The LOR offset $\chi_{j,k} = \eta(\alpha_j) - \eta(\beta_{j,k})$ is estimated for each LOR separately by maximizing the correlation with the measured TOF profile m_{j,k,i_t},

$$\hat{\chi}_{j,k} = \arg\max_{\chi} \left\{ \sum_{i_t} \sum_{i'_t} q_{j,k,i_t} m_{j,k,i'_t} \, b_3 \left(\frac{i_t \Delta_t + \chi - i'_t \Delta_t}{\Delta_t} \right) \right\} \tag{23}$$

where b_3 is the cubic B-spline. We solve the maximization (23) by exhaustive search with steps of 1 mm.

After thus calculating the LOR offsets, the procedure is the same as for other calibration methods, which use a known source to directly measure the LOR offsets $\hat{\chi}$ [11, 12]: the detector offsets η are calculated as the least-squares solution of the set of linear equations

$$\eta_{j_1} - \eta_{j_2} = \hat{\chi}_{j_1, -N+(j_2-j_1)\%(2N)} \quad (j_1, j_2) \in \mathcal{L}_\epsilon \tag{24}$$

for all LORs with enough activity,

$$\mathcal{L}_\epsilon = \{(j_1, j_2) \mid M_{0, j_1, -N+(j_2-j_1)\%(2N)} > \epsilon \max M_0\}. \tag{25}$$

We used $\epsilon = 0.1$ in our implementation. As in section (6.1) we solve (24) by gaussian elimination after adding a diagonal matrix $\mu \, \lambda_{max} \, Id$ with $\mu = 10^{-5}$ to avoid indeterminacy.

7. Simulation

We simulated a single ring scanner of diameter $2R = 842$ mm with $2N = 672$ equally spaced detectors. Timing offsets η were generated for a scanner with 48 blocks of 14 detectors, as the sum of two terms (Fig. 1b). The first term was generated as a uniform random number over the interval $(-25, +25)$ mm. Recall that all times are converted to distance in this paper, this interval corresponds to $(-167, +167)$ ps. The second term was constant in each block and was generated as a uniform random number over the interval $(-30, +30)$ mm. A constant was added to the thus obtained offsets so as to get a zero mean. Each detector was in coincidence with a fan of 301 detectors ($k_{max} = 150$) covering a field-of-view of radius $R_{FOV} = 272$ mm. The LOR offsets were then computed as the difference between the offsets of the two detectors in coincidence.

We simulated 2D TOF data for the phantom in Fig.1a using an analytic line integral model. Each LOR was obtained as the average of 81 line integrals to roughly mimick the effect of the detector width. The TOF resolution was 52.5 mm FWHM (corresponding to 350 ps), and data were binned with 40 TOF bins of width $\Delta_t = 16$ mm, with the center of each time bin shifted by the corresponding TOF offset computed as described above. Exact correction for attenuation, scatter and random background, and sensitivity was assumed.

The TOF offsets were estimated from noise-free data and from a noisy data set with maximum data bin count of 14, corresponding to a total of $N_{events} = 7.4\ 10^6$ true coincidences. Poisson noise was added to the attenuated data, which were then corrected for attenuation before estimating the TOF offsets. The attenuation coefficient was 0.0966 cm^{-1} except in the lungs (excluding the two lung tumors) where it was 0.0166 cm^{-1}. We simulated 90 independent realizations of the noisy data to estimate the variance and the bias. Estimating the bias (equal to the difference between the average value of the estimated offsets and their true value) is important for this non-linear TOF calibration problem because the average value of the estimated offsets is not necessarily equal to the offsets computed from noise-free data.

The detector offsets were estimated using the fan- and TOF-summed relation (13). Before applying (13), M_0 was smoothed for the noisy data as described in section 6.2, but for the noise-free data the smoothing was not applied. One exception are the data in Table 2, which illustrate the effect of the smoothing. As a reference the offsets were also estimated using the indirect method, with a non-penalized OSEM reconstruction (8 subsets, 8 iterations) of the summed TOF data (M_0) on a 256×256 pixel grid with pixel size 2.054 mm.

For each method, the LOR offsets $\hat{\eta}(\alpha) - \hat{\eta}(\beta)$ were calculated for the 672×301 LORs as differences between the estimated detector offsets. These "denoised" estimates of the LOR offsets were compared to the exact simulated values.

7.1. Noise-free data without gaps

First we illustrate the accuracy of the consistency based method and of the indirect method in the ideal case of noise free data and in the absence of detector gaps. Fig. 2a shows that in that case the error on the estimated offsets does not exceed 2 mm and remains therefore much smaller than the TOF resolution (52.5 mm). A similar observation holds for the error on estimated denoised LOR offsets (Table 1).

7.2. Application in the presence of gaps

We repeated the simulation for a scanner consisting of 48 blocks of 14 detectors, with one gap of one detector in each block. Thus the detectors $j = 14k$ are missing for $k = 0 \ldots 47$. The object and the simulated timing misalignement were the same as in section 7.1 (Fig. 1). All images were reconstructed on a 256×256 grid with pixel size

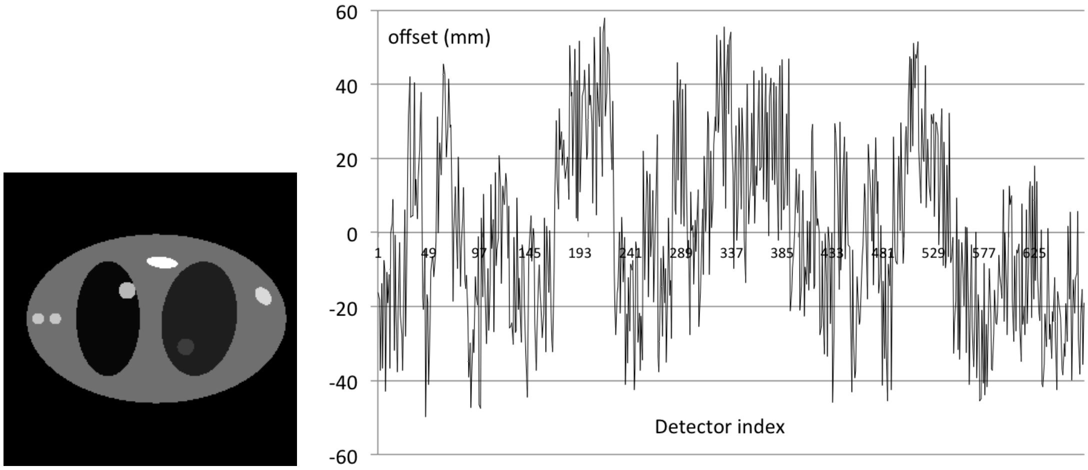

(a) (b)

Figure 1: (a): The thorax phantom is supported in an ellipse with axes 300 mm and 461 mm.(b): The simulated offsets η_j (in mm) for the 672 detectors. The vertical scale $(-60, +60)$ mm corresponds to $(-400, +400)$ ps.

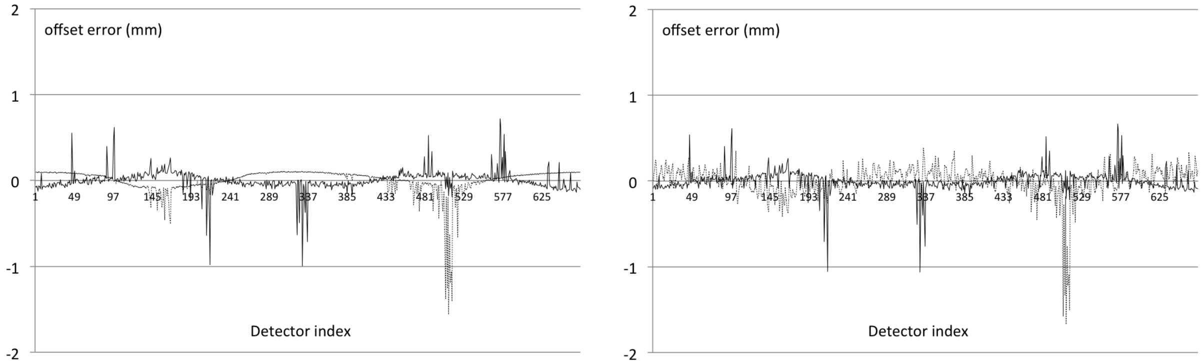

(a) (b)

Figure 2: The error $\hat{\eta} - \eta$ (in mm) for the 672 detector offsets estimated using equation (13) (dotted line) and the indirect method (full line). The horizontal axis is the detector index and the points are linked by a continuous curve. (a) noise free data without gaps (b) noise free data with gaps: the ring has 48 blocks each with a gap of one detector.

Table 1: Maximum error, mean L^2 error (RMS), and mean L^1 error for the LOR offsets $\chi_{j,k} = \eta(\alpha_j) - \eta(\beta_{j,k})$ estimated from noise free data without gaps (in mm).

		max error	L^2 error	L^1 error
noise free	Eq. (13)	1.66	0.22	0.11
	Indirect	1.72	0.17	0.10

2.054 mm, by applying OSEM with 8 subsets and 8 iterations to the data with gaps, without filling the gaps by interpolation prior to applying OSEM.

The comparison of the error on the detector offsets estimated from noise free

Table 2: Maximum error, mean L^2 error (RMS), and mean L^1 error for the LOR offsets $\chi_{j,k} = \eta(\alpha_j) - \eta(\beta_{j,k})$ estimated from noise free data and from one noisy data set (in mm). The ring has 48 blocks each with a gap of one detector. The consistency based method is here applied with and without smoothing M_0. In all other data in the paper, smoothing is only applied for the noisy data.

		max error	L^2 error	L^1 error
noise free	Eq. (13), no smooth	2.02	0.27	0.15
	Eq. (13), smooth M_0	1.76	0.29	0.19
	Indirect	1.73	0.18	0.10
noisy data	Eq. (13), no smooth	19.90	4.69	3.47
	Eq. (13), smooth M_0	14.63	3.40	2.52
	Indirect	3.79	0.69	0.50

data without (Fig.2a) and with (Fig.2b) gaps shows that the indirect method and the consistency based method are only marginally degraded by the gaps.

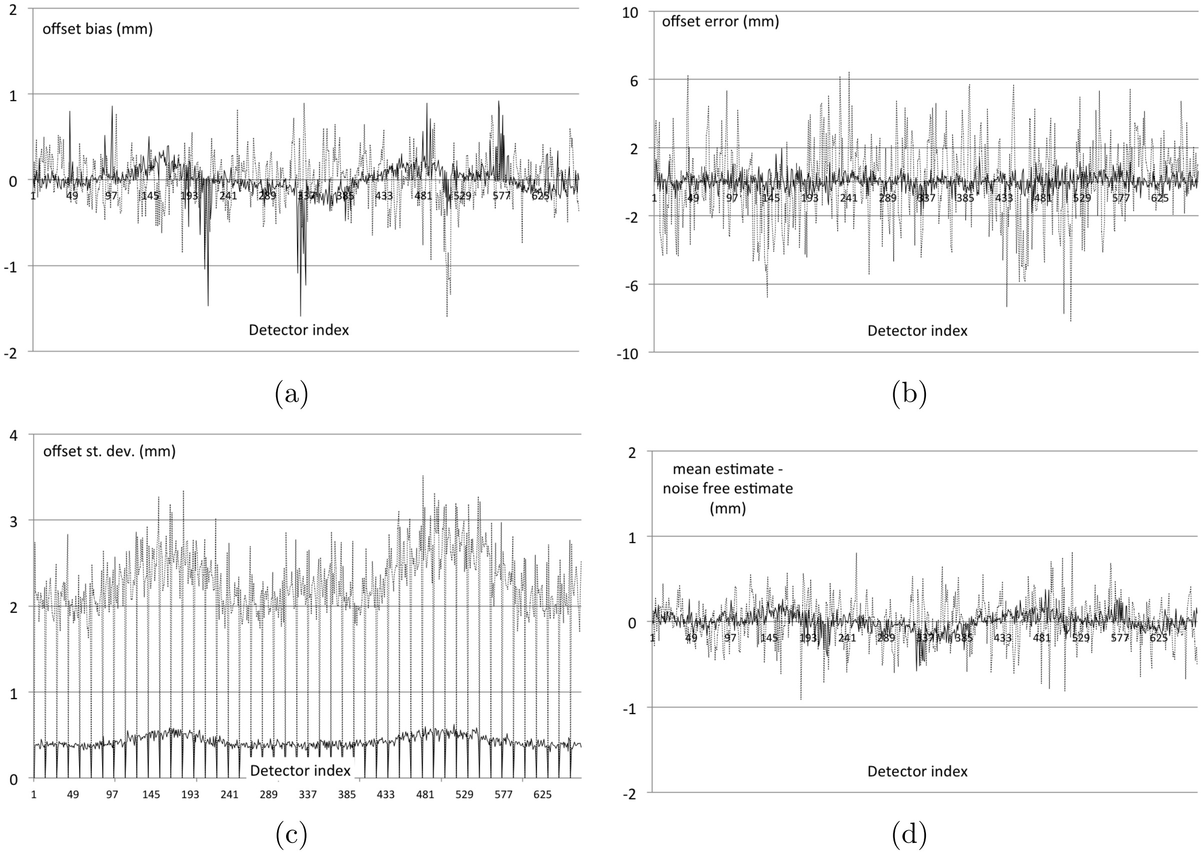

(a) (b)

(c) (d)

Figure 3: The error $\hat{\eta} - \eta$ (in mm) for the detector offsets estimated using (13, dotted line) and the indirect method (full line). The ring has 48 blocks each with a gap of one detector. Noisy data, $7.4\,10^6$ events. (a) Bias (mean error of the 90 noise realizations). (b) Error for one of the noisy data sets. (c) Standard deviation of the estimated offsets (sample standard deviation of the 90 noise realizations). (d) Difference between the sample mean estimates in (a) and the noise free estimates of Fig.2b. Note the different vertical scales in each plot.

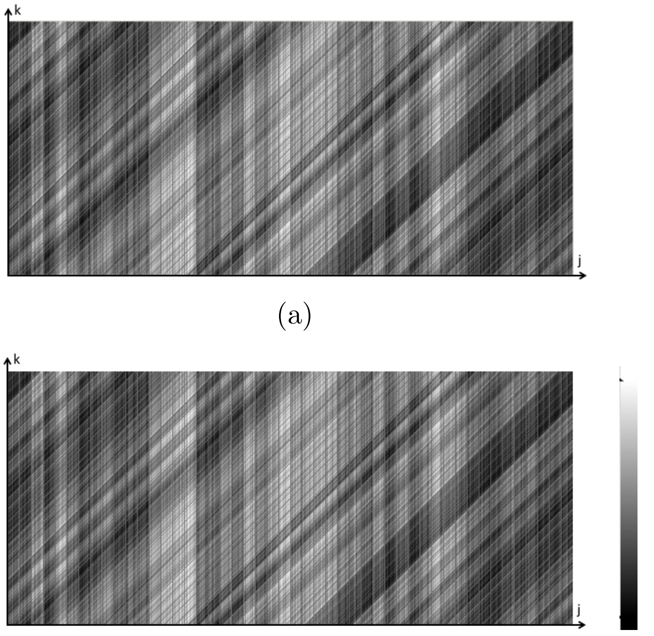

(a)

(b) (c)

Figure 4: The LOR offsets $\chi_{j,k} = \eta(\alpha_j) - \eta(\beta_{j,k})$. The ring has 48 blocks each with a gap of one detector. The horizontal axis is the detector index j, the vertical axis is the fan index k (see equation (18)). (a) The simulated offsets. (b) The offsets estimated using the consistency relation (13) with one of the noisy data sets ($7.4\,10^6$ events). (c) Grey scale $(-100, +100)$ mm. The gaps appear as regularly spaced constant vertical and diagonal lines.

Figure 3 shows the results with gaps and noisy data. The standard deviation is about five times larger with the consistency based method than with the indirect method. Fig.3d shows the difference between the mean values and the offsets (Fig.2b) estimated from noise free data. These differences are small compared to the bias in Fig.3a, suggesting that the bias caused by the non-linear nature of equation (13), if any, is small. Table 2 and Fig.4 give an example of the error on the estimated LOR offsets, for the noise sample corresponding to Fig.3b. Table 2 also shows that the smoothing of M_0 has a small impact on the error for noise-free data, while significantly reducing the variance in the presence of noise.

7.3. Impact on image reconstruction in presence of gaps

Figure 5 shows OSEM reconstructions from noise free data and from one noisy data set in presence of gaps. The results illustrate the small impact on image reconstruction of the lower accuracy of the consistency based method for offset correction compared to the indirect method. This observation is confirmed by the profile in Fig. 6f.

The mean activity in the eight regions of interest (ROI) shown in Fig. 6e was calculated for the images reconstructed from the 90 noisy data sets. Fig. 6 shows the bias and standard deviation of the estimated ROI means. The bias caused by the TOF misalignement is well corrected by the proposed method, the accuracy and precision of which are similar to those of the indirect method for this study. The results for the non-TOF reconstruction are also given for completeness but are difficult to compare because of the slower convergence [13, 14, 15] of non-TOF OSEM. The trade off between bias and standard deviation could be modified by increasing the number of iterations, but the goal of this work is not to compare TOF and non-TOF reconstruction.

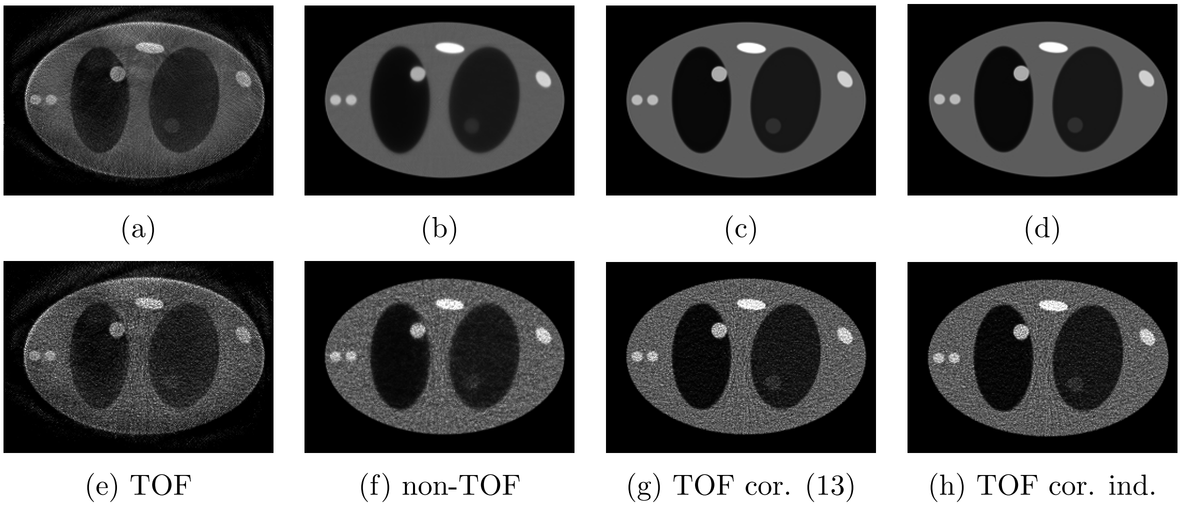
(a) (b) (c) (d)

(e) TOF (f) non-TOF (g) TOF cor. (13) (h) TOF cor. ind.

Figure 5: OSEM reconstruction of the thorax phantom (8 iterations, 8 subsets). The ring has 48 blocks each with a gap of one detector. First row: noise free data. Second row: one of the noisy data sets. (a, e) TOF reconstruction without offset correction, (b, f) non-TOF reconstruction, (c, g) TOF reconstruction with offset corrected using (13), (d, h) TOF reconstruction with offset corrected using the indirect method. Grey scale $(0, 0.55)$.

Despite the non-linearity of the TOF calibration problem, the error on the LOR offsets estimated using the consistency based method follows to a good approximation the $1/\sqrt{N_{events}}$ behaviour typical of linear problem with Poisson data, with N_{events} the total number of true events in the data. This is illustrated by Fig. 7, which shows a log-log plot of the RMS error of the LOR offsets $\hat{\chi}$ versus N_{events}.

7.4. Estimated computation times

The implementation in C runs on a MacBook Pro (2.3 GHz Intel Core I5). For the parameters in this study the computation time for the proposed method is 6.2 s. The computation time for the indirect method is 192 s, including 5.9 s for the non-TOF reconstruction, 180 s for the estimation of the LOR offsets, and 6.0 s for the estimation of the crystal offsets from the LOR offsets (solving (24)). The computation time for the indirect method could be reduced by using fewer TOF bins and/or by using a step size larger than 1 mm when aligning the TOF profiles in (23).

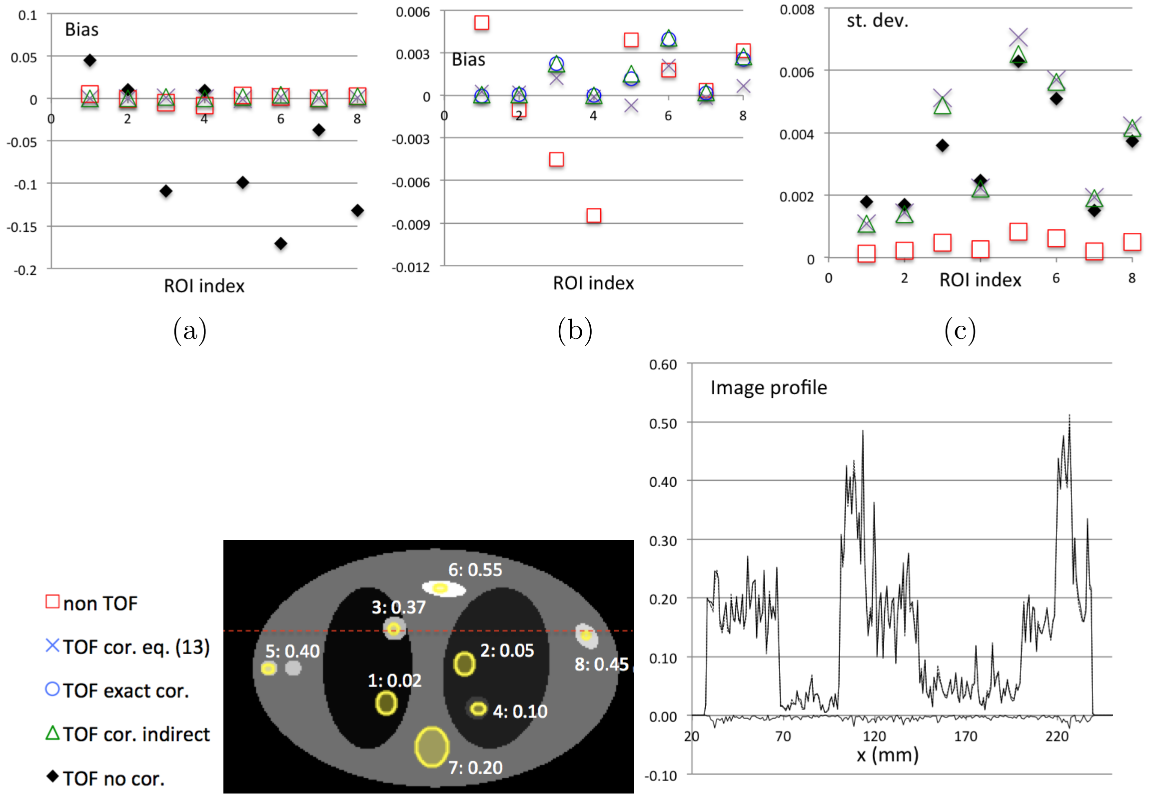

(a) (b) (c)

(d) (e) (f)

Figure 6: OSEM reconstruction of the thorax phantom (8 iterations, 8 subsets) from noisy data with gaps. The horizontal index in the plots corresponds to the eight ROIs shown in the insert (e) and labeled as 'ROI index : exact value'. (a) bias on the estimated ROI mean (mean error of the 90 noise realizations); (b) zoom of (a); (c) standard deviation of the estimated ROI mean (sample standard deviation of the 90 noise realizations). Symbols are shown in insert (d): Red square: non-TOF reconstruction, blue cross: TOF reconstruction with misalignment corrected using (13), blue circles in (b): TOF reconstruction with misalignment corrected by the exact LOR offsets, green triangles: TOF reconstruction with misalignment corrected by the indirect method, black diamonds in (a,c): non corrected TOF reconstruction. (f) Profile of the reconstruction from one of the noisy data along the dashed red line in insert (e). Full line: indirect method, dotted line: eq. (13), bottom line: minus the absolute difference of the two curves.

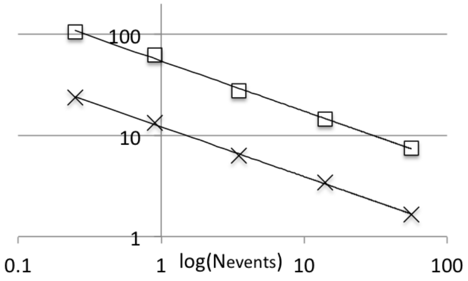

Figure 7: Log-log plot of the RMS error (cross) and maximum error (squares) of the LOR offsets (in mm) estimated from noisy data with gaps using (13), versus the total count in the 2D TOF data (in millions). The best linear fits (lines) have slope $(N_{events})^{-0.493}$ and $(N_{events})^{-0.496}$. A single noisy data set has been used for each point.

8. Conclusions

This paper introduces new data driven methods for the time calibration of TOF PET scanners. These methods are based on the consistency conditions for TOF data and are faster than the indirect method, which requires a preliminary reconstruction from the TOF-summed data. The main goal of the paper is to introduce three equations linking the timing offsets of the detectors to the TOF data. These equations, (6), (7) and (13), all allow estimating the offsets, but we chose to implement equation (13), an integral equation which only involves the TOF summed data (M_0) and the mean TOF (M_1/M_0) of each LOR, and can be easily discretized.

The paper also presents an evaluation with 2D TOF data simulated for a single detector ring circular scanner. The robustness for noise of the indirect method [5] remains unmatched by the consistency based method. However the RMS errors on the TOF offsets estimated by solving (13) remain in all tested cases lower than 10% of the TOF FWHM resolution (tables 1 and 2), and in our simulations this lower accuracy had a small impact on the images reconstructed using OSEM.

The only deviations from ideality in the simulation were

- the TOF misalignments,
- the imperfect match between the simulation model and the projector for the OSEM reconstruction,
- and the detector gaps.

The influence of the scatter and random background on the relative accuracy of the indirect and new methods remains to be evaluated. Especially scatter is an issue because model based scatter calculations require an initial estimate of the activity image, which is precisely what the proposed calibration methods allow to bypass.

The noisy 2D data set in section 7 corresponds to 7 million trues, a rather large value for a single slice. We expect however that generalizing the proposed method to 3D will lead to an improved variance because the offset of each detector would then be estimated using a larger number of LORs connecting it to several detector rings. The systematic errors caused by the gaps and the discretization are not expected to undergo large modifications in 3D, but these errors were not dominant in our 2D study. Verifying these conjectures will require extending the proposed TOF calibration to 3D PET by applying the same approach to the 3D consistency conditions (equations (5) and (6) in [20]). Although equation (7) can be generalized to 3D, the axial truncation would lead to the presence of boundary terms when integrating this equation over β as in section 5. A second potential issue in 3D is the larger dimension of the system of linear equations (section 6.1), which is equal to the number of detectors (not the number of LORs). When the number of detector rings is large this may necessitate an implementation over overlapping subsets of rings.

No regularization was applied in this work. Several techniques could potentially improve the stability in presence of noise. One approach, explored by Freeze et al in the same context [16], replaces the least-squares estimation by L_1 minimization to improve the robustness to outliers. A second option is a standard regularization by penalized least-squares estimation. For instance Yu et al [4] apply a total variation penalty on the detector offsets within each detector block. It is difficult however to identify an appropriate regularizing penalty because the detector offsets are not smooth. A third approach would be to solve the full consistency equation (6) instead of integrating over the TOF and fan angle variables as we did for the numerical tests. Besides the increased numerical complexity, a potential pitfall of solving (6) is a bias caused by the non-linearity of the resulting discretized system of equations. A total least squares method [21] might then be preferable to the least squares approach used in this paper.

Acknowledgments

This work was supported by the Project G027514N of the Fonds Wetenschappelijk Onderzoek Vlaanderen (FWO) and by the Strategic Research Program SRP10 of the VUB. A. Rezaei is a posdoctoral fellow of the FWO project 12T7118N.

Appendix 1: Proof of the consistency condition (5)

We give a direct proof of the consistency equation starting from (2). Define the derivatives $\partial\vec{a}/\partial\alpha = \vec{a}^\perp = (-R\sin\alpha, R\cos\alpha)$, $\partial\vec{b}/\partial\beta = \vec{b}^\perp = (-R\sin\beta, R\cos\beta)$, and

$$\partial L/\partial\alpha = -\vec{b}\cdot\vec{a}^\perp/L = \sin(\alpha-\beta)\,R^2/L = -\partial L/\partial\beta. \tag{26}$$

The derivatives of the ideal data (2) are:

$$\begin{aligned}
\frac{\partial q}{\partial\alpha} &= \int dl\, w(t-l)\Big(\frac{\vec{a}^\perp}{2} - l\frac{\vec{a}^\perp}{L} - l\frac{\vec{a}-\vec{b}}{L^3}(\vec{b}\cdot\vec{a}^\perp)\Big)\cdot(\nabla f)\\
\frac{\partial q}{\partial\beta} &= \int dl\, w(t-l)\Big(\frac{\vec{b}^\perp}{2} + l\frac{\vec{b}^\perp}{L} + l\frac{\vec{a}-\vec{b}}{L^3}(\vec{b}\cdot\vec{a}^\perp)\Big)\cdot(\nabla f)\\
\frac{\partial q}{\partial t} &= \int dl\, w(t-l)\,\frac{(l-t)}{\sigma^2}\,f\\
\frac{\partial^2 q}{\partial\alpha\partial t} &= \int dl\, w(t-l)\,\frac{(l-t)}{\sigma^2}\Big(\frac{\vec{a}^\perp}{2} - l\frac{\vec{a}^\perp}{L} - l\frac{\vec{a}-\vec{b}}{L^3}(\vec{b}\cdot\vec{a}^\perp)\Big)\cdot(\nabla f)\\
\frac{\partial^2 q}{\partial\beta\partial t} &= \int dl\, w(t-l)\,\frac{(l-t)}{\sigma^2}\Big(\frac{\vec{b}^\perp}{2} + l\frac{\vec{b}^\perp}{L} + l\frac{\vec{a}-\vec{b}}{L^3}(\vec{b}\cdot\vec{a}^\perp)\Big)\cdot(\nabla f)
\end{aligned} \tag{27}$$

where the argument of f and its gradient ∇f is everywhere as in (2), and w is the gaussian TOF profile (3). We also note that

$$\begin{aligned}
0 &= \int dl\,\frac{d}{dl}\left\{ w(t-l)\, f\Big(\frac{\vec{a}+\vec{b}}{2} - l\frac{\vec{a}-\vec{b}}{L}\Big)\right\}\\
&= \int dl\, w(t-l)\left\{\frac{(t-l)}{\sigma^2}\, f - (\nabla f)\cdot\frac{\vec{a}-\vec{b}}{L}\right\}.
\end{aligned} \tag{28}$$

Inserting the derivatives (27) into (5), using $L/2 = R|\sin(\frac{\beta-\alpha}{2})|$, and subtracting $R^2\cos((\beta-\alpha)/2)\times$ (28), we obtain

$$\mathcal{E}q = \int dl\, w(t-l)\, \frac{R^2(L^2-4l^2)}{L^3}\,(\nabla f)\cdot\left\{\sin(\frac{\beta-\alpha}{2})(\vec{a}^{\perp}+\vec{b}^{\perp}) + \cos(\frac{\beta-\alpha}{2})(\vec{a}-\vec{b})\right\} \quad (29)$$

One verifies by direct calculation that the vector in curly brackets is identically zero, and therefore $\mathcal{E}q = 0$.

Appendix 2: Proof of the detector offset equation (6)

Applying to m the operator $\mathcal{E}$ defined by (5), and using $m(\alpha,\beta,t) = q(\alpha,\beta,t-\eta(\alpha)+\eta(\beta))$ one obtains:

$$\begin{aligned}\mathcal{E}m &= t\left(\frac{\partial q}{\partial\alpha}-\frac{\partial q}{\partial\beta}\right)\frac{1}{\sin((\beta-\alpha)/2)} + \zeta(\alpha,\beta)\,R\left(\frac{\partial q}{\partial\alpha}+\frac{\partial q}{\partial\beta}\right)\\ &- R^2\cos((\beta-\alpha)/2)\frac{\partial q}{\partial t} + \sigma^2\left(\frac{\partial^2 q}{\partial\alpha\partial t}-\frac{\partial^2 q}{\partial\beta\partial t}\right)\frac{1}{\sin((\beta-\alpha)/2)}\\ &- t\frac{\partial q}{\partial t}\,(\eta'(\alpha)+\eta'(\beta))\,\frac{1}{\sin((\beta-\alpha)/2)} - \zeta(\alpha,\beta)\,R\frac{\partial q}{\partial t}\,(\eta'(\alpha)-\eta'(\beta))\\ &- \sigma^2\frac{\partial^2 q}{\partial t^2}\,(\eta'(\alpha)+\eta'(\beta))\,\frac{1}{\sin((\beta-\alpha)/2)} \qquad (30)\end{aligned}$$

where $\zeta(\alpha,\beta) = sign(\sin((\beta-\alpha)/2))$ and the argument of q and of its derivatives is $(\alpha,\beta,t-\eta(\alpha)+\eta(\beta))$. Now use that q satisfies the consistency condition (5), but with t replaced by $t-\eta(\alpha)+\eta(\beta)$, hence

$$\begin{aligned}0 &= (t-\eta(\alpha)+\eta(\beta))\left(\frac{\partial q}{\partial\alpha}-\frac{\partial q}{\partial\beta}\right)\frac{1}{\sin((\beta-\alpha)/2)} + \zeta(\alpha,\beta)\,R\left(\frac{\partial q}{\partial\alpha}+\frac{\partial q}{\partial\beta}\right)\\ &- R^2\cos((\beta-\alpha)/2)\frac{\partial q}{\partial t} + \sigma^2\left(\frac{\partial^2 q}{\partial\alpha\partial t}-\frac{\partial^2 q}{\partial\beta\partial t}\right)\frac{1}{\sin((\beta-\alpha)/2)}. \qquad (31)\end{aligned}$$

Subtracting (31) from (30),

$$\begin{aligned}\mathcal{E}m &= (\eta(\alpha)-\eta(\beta))\left(\frac{\partial q}{\partial\alpha}-\frac{\partial q}{\partial\beta}\right)\frac{1}{\sin((\beta-\alpha)/2)}\\ &- t\frac{\partial q}{\partial t}\,(\eta'(\alpha)+\eta'(\beta))\,\frac{1}{\sin((\beta-\alpha)/2)} - \zeta(\alpha,\beta)\,R\frac{\partial q}{\partial t}\,(\eta'(\alpha)-\eta'(\beta))\\ &- \sigma^2\frac{\partial^2 q}{\partial t^2}\,(\eta'(\alpha)+\eta'(\beta))\,\frac{1}{\sin((\beta-\alpha)/2)}. \qquad (32)\end{aligned}$$

Finally (6) is obtained by replacing again q by m in the RHS of (32), noting that $q(\alpha,\beta,t) = m(\alpha,\beta,t+\eta(\alpha)-\eta(\beta))$ and hence

$$\frac{\partial q}{\partial\alpha} = \frac{\partial m}{\partial\alpha} + \frac{\partial m}{\partial t}\eta'(\alpha) \quad ; \quad \frac{\partial q}{\partial\beta} = \frac{\partial m}{\partial\beta} - \frac{\partial m}{\partial t}\eta'(\beta). \qquad (33)$$

Appendix 3: Proof of the TOF-summed equation (7)

Equation (7) is obtained by integrating (6) over $t_{min} \leq t \leq t_{max}$, using the definition (5) of $\mathcal{E}$ for the LHS, and the identities

$$0 = \int_{t_{min}}^{t_{max}} dt\, \frac{\partial m}{\partial t} = \int_{t_{min}}^{t_{max}} dt\, \frac{\partial^2 m}{\partial t^2} = \int_{t_{min}}^{t_{max}} dt\, \frac{\partial^2 m}{\partial \alpha \partial t} = \int_{t_{min}}^{t_{max}} dt\, \frac{\partial^2 m}{\partial \beta \partial t}$$
$$0 = \int_{t_{min}}^{t_{max}} dt\, \frac{\partial}{\partial t}(tm) = \int_{t_{min}}^{t_{max}} dt\, t\, \frac{\partial m}{\partial t} + \int_{t_{min}}^{t_{max}} dt\, m \qquad (34)$$

Due to the infinite support of the TOF profile w, these identities only hold, strictly, if $-t_{min} = t_{max} = \infty$. However they remain accurate provided the sampled interval $t_{min} \leq t \leq t_{max}$ covers the support of the activity distribution, enlarged by a few FWHMs.

Appendix 4: Proof of the invariance property (10)

Equation (10) is obtained by integrating (7) at fixed α over the full fan $\alpha + \pi - \Phi \leq \beta \leq \alpha + \pi + \Phi$. The assumption that the projections are not truncated and have no gaps enables to integrate by part with vanishing boundary terms. We give here an alternative proof, which provides a relation between f and the constant C in (10) and shows that the relation holds for any TOF profile such that

$$\int_{-\infty}^{\infty} dt\, w(t) = 1 \quad ; \quad \int_{-\infty}^{\infty} dt\, t\, w(t) = 0. \qquad (35)$$

We assume that $-t_{min} = t_{max} = \infty$. First rewrite the ideal data (2) as

$$q(\alpha, \beta, t) = \int dl\, w(t - l)\, f\Big(\vec{a} + (l + \frac{L}{2})\, \hat{n}(\alpha, \beta)\Big) \qquad (36)$$

with the unit vector along the LOR,

$$\hat{n}(\alpha, \beta) = \frac{\vec{b} - \vec{a}}{L}. \qquad (37)$$

Recall that the misaligned data are $m(\alpha, \beta, t) = q(\alpha, \beta, t - \chi(\alpha, \beta))$ with LOR offset $\chi(\alpha, \beta) = \eta(\alpha) - \eta(\beta)$. The moments of the TOF data are then

$$M_i(\alpha, \beta) = \int_{-\infty}^{\infty} dt\, t^i \int_{-\infty}^{\infty} dl\, w(t - \chi(\alpha, \beta) - l)\, f\Big(\vec{a} + (l + \frac{L}{2})\, \hat{n}(\alpha, \beta)\Big) \quad i = 0, 1. (38)$$

Changing the integration variables to $t' = t - \chi(\alpha, \beta) - l$ and $l' = l + L/2$, and noting that with $-t_{min} = t_{max} = \infty$ the integration interval is invariant, the first moment becomes

$$M_1(\alpha, \beta) = \int_{-\infty}^{\infty} dt' \int_{-\infty}^{\infty} dl'\, (t' + \chi(\alpha, \beta) + l' - L/2)\, w(t')\, f\Big(\vec{a} + l'\, \hat{n}(\alpha, \beta)\Big)$$
$$= (\chi(\alpha, \beta) - \frac{L}{2}) M_0(\alpha, \beta) + \int_{0}^{\infty} dl'\, l'\, f\Big(\vec{a} + l'\, \hat{n}(\alpha, \beta)\Big) \qquad (39)$$

where we used (35) and changed the lower bound of the l' integral to 0 because the support of f is within the detector ring. Integrate (39) with respect to β at fixed

α and note‡ that $(\beta-\alpha)/2, l'$ are polar coordinates centered at $\vec{a}$. Replacing L by its expression (1), and using the assumption that the measured fan covers the whole support of the activity, one obtains,

$$\int_{\alpha+\pi-\Phi}^{\alpha+\pi+\Phi} d\beta \left\{ M_1(\alpha,\beta) - \chi(\alpha,\beta) M_0(\alpha,\beta) + R |\sin(\frac{\beta-\alpha}{2})| \, M_0(\alpha,\beta) \right\} =$$

$$\int_{\alpha+\pi-\Phi}^{\alpha+\pi+\Phi} d\beta \int_0^\infty dl' \, l' \, f\Big(\vec{a} + l' \, \hat{n}(\alpha,\beta)\Big) = 2 \int_{\mathbb{R}^2} d\vec{x} f(\vec{x}). \qquad (40)$$

The RHS is independent of α, and this completes the proof of (10).

Appendix 5: Uniqueness

We show in this section that the fan- and TOF summed equation (13) has only one solution up to an additive constant. Therefore the two first moments M_0 and M_1 of the pre-corrected data contain enough information to determine the detector offsets up to a constant§.

The proof below uses the following assumptions:

(i) $\eta \in C^1(0,2\pi)$ and $M_0, M_1 \in C^1((0,2\pi)\times(0,2\pi))$.

(ii) $M_0(\alpha,\beta) \geq 0$, $\alpha,\beta \in [0,2\pi)$.

(iii) The fan covers the object, hence $M_0(\alpha,\beta), M_1(\alpha,\beta)$ and their derivatives are zero at $\beta = \alpha + \pi \pm \Phi$.

(iv) $T(\alpha) = \int M_0(\alpha,\beta) d\beta \geq T_{min}$ for some $T_{min} > 0$ and $\alpha \in [0,2\pi)$.

(v) Any pair of detectors $\alpha_1, \alpha_2 \in [0,2\pi)$ can be connected via a sequence of detectors $\alpha_1 = \gamma_1 \to \gamma_2 \to \ldots \to \gamma_n = \alpha_2$ such that $M_0(\gamma_{j+1},\gamma_j) > 0$ for $j = 1,\ldots,n-1$.

The first assumption is required by the continuous framework used in this note. Assumptions (ii),(iii),(iv) are obvious physical conditions. The last assumption means that two detectors can be connected by a sequence of active LORs; one easily checks that this condition is verified unless the object consists of a finite set of point sources.

Proof. According to the theorem of the alternative of Fredholm [17, 18], the integral equation of the second type with continuous kernels, (13), has a unique solution up to a constant if the only solutions of the homogeneous equation

$$0 = T(\alpha)\,\eta(\alpha) - \int_0^{2\pi} d\beta \, K(\alpha,\beta)\eta(\beta) \quad 0 \leq \alpha < 2\pi \qquad (41)$$

are constant. We now prove this property for our problem, with the kernel K equal to the symmetric extension (16) of the TOF summed data M_0. Suppose some function

---

‡ The factor 1/2 stems from the usual property of the circle that the angle at the center (here, β) is twice the angle at the circumference (here the required polar angle).

§ Note that the uniqueness result holds a fortiori if one uses the full equation (6), because it exploits the full TOF information, whereas the proof only uses the TOF summed data M_0 and M_1.

$\eta \in C^1(0, 2\pi)$ is a solution of (41). Multiplying (41) by $\eta(\alpha)$, replacing $T(\alpha)$ by its definition (14) , and integrating over α, one has

$$\begin{aligned} 0 &= \int_0^{2\pi} d\alpha\, \eta(\alpha) \int_0^{2\pi} d\beta\, \{\eta(\alpha) M_0(\alpha,\beta) - \eta(\beta) M_0(\alpha,\beta)\} \\ &= \frac{1}{2} \int_0^{2\pi} d\alpha \int_0^{2\pi} d\beta\, (\eta(\alpha) - \eta(\beta))^2\, M_0(\alpha,\beta). \end{aligned} \tag{42}$$

We used the symmetry $M_0(\alpha,\beta) = M_0(\beta,\alpha)$. Since $\eta \in C^1$, $M_0 \in C^1$, and $M_0 \geq 0$, it follows from (42) that $\eta(\alpha) = \eta(\beta)$ for all LORs such that $M_0(\alpha,\beta) > 0$. Using assumption (v) one can propagate this result to all detectors. This concludes the proof that the only solutions of the homogeneous equation are equal to a constant.

9. References

[1] Perkins A E, Werner M, Kuhn A, Surti S, Muehllehner G and Karp J S 2005 Time-of-flight coincidence timing calibration techniques using radioactive sources, *IEEE Nucl. Sci. Symp. Conf. Rec.* vol 5 pp 2488-91.

[2] Thompson C J, Camborde M and Casey M E 2005 A central positron source to perform the timing alignment of detectors in a PET scanner, *IEEE Trans. Nucl. Sci.* 52 1300-4.

[3] Li X, Burr K C, Wang G-C, Du H and Gagnon D 2016 Timing Calibration for Time-of-Flight PET Using Positron-Emitting Isotopes and Annihilation Targets, *IEEE Trans. Nucl. Sci.* 63 1351-1358.

[4] Yu X, Isobe T, Watanabe M and Liu H 2016 Novel crystal timing calibration method based on total variation, *Phys. Med. Biol.* 61 7833-7847.

[5] Werner M E and Karp J S 2013 TOF PET offset calibration from clinical data, *Phys. Med. Biol.* 58 4031-46.

[6] Rezaei A, Schramm G and Nuyts J 2017 Data driven time alignment for TOF-PET, *Records of the 2017 IEEE Medical Imaging Conference, Atlanta (GA).*

[7] Jinghan Ye and Xiyun Song 2016 detector timing offset calibration method for time of flight PET scanners, *Proc. SPIE 9783, Medical Imaging 2016: Physics of Medical Imaging*, 97831M (2016/03/25);

[8] Panin V Y, Defrise M, Casey M E 2010 Restoration of fine azimuthal sampling of measured TOF projection data, *Records 2010 IEEE Nuclear Science Symposium and Medical Imaging Conference, Knoxville*, paper M17-4

[9] Defrise M, Rezaei A, Nuyts J 2012 Time-of-flight PET determine the attenuation sinogram up to a constant, *Phys. Med. Biol.* 57 885-899.

[10] Joseph P M 1982 An Improved Algorithm for Reprojecting Rays Through Pixel Images, *IEEE Trans. Med. Imag.* 1 192-196.

[11] Park S-J, Southekal S, Purschke M, Junnarkar S S, Pratte J-F, Stoll S P, Woody C L, Schlyer D J, and Vaska P 2008 Digital Coincidence Processing for the RatCAP Conscious Rat Brain PET Scanner, *IEEE Trans. Nucl. Sci.* 55 510-515.

[12] Mann A B, Paul S, Tapfer A, Spanoudaki V C and Ziegler S I 2009 A Computing Efficient PET Time Calibration Method Based on Pseudoinverse Matrices, *IEEE Nucl. Sci. Symp. Conf. Rec.* pp. 3889-3892.

[13] Surti S, Karp J S, Popescu L M, Daube-Witherspoon M E, Werner M 2006 Investigation of Time-of-Flight Benefit for Fully 3-D PET, *IEEE Trans. Med. Imag.* 25 pp. 529-38.

[14] Watson C C 2006 Image Noise Variance in 3D OSEM Reconstruction of Clinical Time-of-Flight PET, 2006 IEEE Nucl. Sci. Symp. Conf. Rec. pp. 1736-1739.

[15] Kadrmas D J, Casey M E, Conti M, Jakoby B W, Lois C and Townsend D W 2009 Impact of Time-of-Flight on PET Tumor Detection, *J. Nucl. Med.* 50 pp. 1315-1323.

[16] Freeze D L, Hsu D F C, Innes D and Levin C S 2017 Robust timing calibration for PET using L1-norm minimization, *IEEE Trans. Med. Imag.* 36 pp. 1418-1426.

[17] Kress R, Linear integral equations, Springer 1999.

[18] Tricomi F G, Integral equations, Dover 1985.

[19] Press W H, Teukolsky S A, Vetterling W T and Flannery B P, Numerical Recipes in C, Cambridge University Press 1994.

[20] Defrise M, Panin V Y, Michel C and Casey M E, Continuous and discrete data rebinning in time-of-flight PET, *IEEE Trans. Med. Imag.* 27 pp. 1310-22 (2008).

[21] Van Huffel and Vandewalle J, The Total Least Squares Problem. Society for Industrial and Applied Mathematics, 1991.